ZnAl2O4 as potential sensor : variation of luminescence with thermal history

Lucile Cornu, Manuel Gaudon, Veronique Jubera

$ZnAl_2O_4$ as potential sensor : variation of luminescence with thermal history.

Authors : Cornu L., Gaudon M. and Jubera V.

Abstract : $ZnAl_2O_4$ spinel powders were prepared using the Pechini or co-precipitation synthetic route and were then treated at different temperatures (600–1350 °C). These powders were characterised by X-ray diffraction, scanning electron microscopy (SEM), diffuse reflectance and luminescence measurements. SEM investigations and the X-ray patterns showed that the spinel crystallite size was dependent on the synthetic route and the treatment temperature. In addition, the structural evolution was investigated by Rietveld refinements. The inversion rate decrease was correlated with the temperature, leading to a direct spinel phase for the sample treated at high temperature. Furthermore, luminescence measurements showed various emissions linked to the presence of defects in the matrix structure. The two main emissions observed were attributed to oxygen vacancy and Zn in the interstitial positions (as revealed by differential Fourier maps). The luminescence spectra exhibited strong differences between 1200 °C and 1350 °C. At the higher temperature, the characteristic emission spectra can be attributed to the direct spinel phase. The indirect–direct spinel transformation can be monitored through the change in the optical properties and correlated to the thermal history of the sample.

Introduction

$ZnAl_2O_4$ spinel compounds have been widely studied: the keyword search "$ZnAl_2O_4$" in the Scopus database produces 460 hits. This material is useful in catalysis for automobiles (either as an active material[1,2] or mainly as a catalytic support[3,4]), as a transparent conductive oxide,[5] as a sintering aid reagent for alumina ceramic[6] and for its dielectric properties.[7,8] Pure $ZnAl_2O_4$ and Ag-doped $ZnAl_2O_4$ are of interest for their photo-catalytic properties.[9,10] Doping with rare earth (RE^{3+}) elements leads to photophysical properties that have potential applications in up-conversion lasers.[11] Cobalt-doped $ZnAl_2O_4$ is widely used as a blue pigment in glass or ceramic,[4,12–15] and the nickel-doped analogue is used as a green-blue pigment, depending on the nickel concentration.[16,17]

$ZnAl_2O_4$ is a wide band gap (3.8 eV) semi-conductor;[18] as such, this material does not absorb at wavelengths higher than 325 nm. This compound is thus an appropriate white host matrix for doping with phosphor cations for photo-emission applications. Consequently, one of the most extensively studied properties of doped $ZnAl_2O_4$ compounds is their photoluminescence. Cr^{3+}-doped $ZnAl_2O_4$ luminescence is widely known,[18–20] as is Mn^{2+} luminescence[21] or RE^{3+} luminescence in such spinel matrices; doping with Eu^{3+},[22] Er^{3+}/Yb^{3+} (ref. 23) or Tb^{3+} (ref. 24) can also be found. Unfortunately, it is apparent from recent investigations that to consider the $ZnAl_2O_4$ matrix as a "white material" is erroneous. The pure $ZnAl_2O_4$ matrix (without any doping) was shown to exhibit luminescence properties when synthesised as small particles;[25] in addition, the absorption properties of $ZnAl_2O_4$ in the UV-visible range and the opto-mechanical effects have been discussed in the literature.[5]

Three families of spinel compounds can be distinguished based on the oxidation states of the metals. The "II–III" family corresponds to oxidation states of A(II) and B(III), and the "IV–II" and "I–VI" families also exist.[26] $ZnAl_2O_4$ belongs to the "II–III" family and is also called gahnite. The $ZnAl_2O_4$ spinel structure is crystalline and belongs to the $Fd\bar{3}m$ space group with a cubic symmetry. Each unit cell is composed of eight AB_2O_4 patterns. The unit cell contains 32 oxygen atoms, which form 64 tetrahedral sites and 32 octahedral sites. In the direct spinel structure, only 8 of the tetrahedral sites (Wyckoff positions 8a (1/8, 1/8, 1/8)) and 16 of the octahedral sites (Wyckoff positions 16d (1/2, 1/2, 1/2)) are respectively occupied by A and B cations. The oxygen atoms fully occupy the 32e positions.[27] Nevertheless, in the composition of $ZnAl_2O_4$, non-negligible equal proportions of A (Zn^{2+}) in the 16d Wyckoff position and B (Al^{3+}) in the 8d position can be reached. The proportion of A in the octahedral site is named the inversion rate δ, and describes the cation distribution in the structure. The general formula of the spinel structure can be written as $(A_{1-\delta}B_\delta)[B_{2-\delta}A_\delta]O_4$. Within the literature, $ZnAl_2O_4$ compounds have been characterised with inversion rates of $0 < \delta < 0.05$.[28–30] It was previously shown that the synthesis temperature can modify the cation distribution (the inversion rate δ) in $ZnAl_2O_4$ spinel structures.[31] Hence, it is very interesting to gauge the effect of different synthetic processes on the cationic distribution. Many synthetic routes to pure $ZnAl_2O_4$ of various particle size have been reported in the literature, such as solid-state reactions,[32–34] tartaric complex formation as the oxide precursor,[35] microwave-assisted hydrothermal processes,[36] autocombustion using glycine/urea fuels,[37,38] sol–gel methods[27] and the Pechini route.[39,40]

In this paper, the co-precipitation technique and the Pechini route with various final thermal treatments are compared, and the correlation of the luminescence properties of $ZnAl_2O_4$ to its structure (inversion rate, presence of defects) is investigated.

Experimental

1-Synthesis of compounds

Two synthetic processes are compared: the Pechini route and co-precipitation. These two processes are illustrated in Fig. 1.
For samples synthesised by the co-precipitation method, stoichiometric amounts of zinc nitrate hexahydrate (Alfa-Aesar, Puratronic 99.998% (metal basis)) and aluminum nitrate nonahydrate (Alfa-Aesar, low mercury, Puratronic 99.999% (metal basis)) were dissolved in aqueous solution to achieve a zinc concentration of 0.8 mol L^{-1}. Aqueous ammonia was then added until a pH of 8.45 was reached. The solution was centrifuged, and the precipitate was dried in an oven at 100 °C for 5 h. In the second step, various thermal treatments were performed between 600 °C and 1200 °C under an air atmosphere.

For the co-precipitation process, the aim is to obtain an amorphous nanoscale precipitate of zinc oxide and aluminum hydroxide. With this method, the difficulty is in producing a simultaneous and complete co-precipitation of both the Zn^{2+} and Al^{3+} cations, which are introduced into solution as a result of the increased pH. ZnO and $Al(OH)_3$ are known to exhibit amphoteric character. Consequently, the adequate pH window for the co-precipitation is very narrow. Indeed, as shown in Fig. 2, an optimal pH of 8.4 was determined, which allows the complete precipitation of both cations.

For the Pechini route, the same metal reagents were used and dissolved in aqueous solution at the same concentrations as in the co-precipitation process. This cationic solution was added to a second aqueous solution of polymeric precursors (citric acid (CA) and ethylene glycol (EG)). This Pechini solution contained a molar ratio of 1 : 4 : 4 salts : CA : EG. This solution enables the polyesterification of EG and CA and the formation of a viscous brown resin by heating to remove excess solvent. A highly viscous mixture was thus obtained, and while a gel was being formed, it was treated at 400 °C under air for 5 hours to lead to a black amorphous powder. In the second step, various thermal treatments of this black residue were performed between 600 °C and 1350 °C under an air atmosphere. In contrast to the co-precipitation process, the Zn : Al target ratio can be set at 1 : 2 in the final spinel structure because there is no possibility of changing the stoichiometry from the starting solution to the final product.

2 X-ray diffraction analysis

Powder X-ray diffraction patterns were collected on a Philips X'Pert MPD X-ray diffractometer with a Bragg–Brentano geometry using Cu $K\alpha_{1,2}$ radiation ($10 < 2\theta < 130°$, step 0.02° and counting time of 30 s). The diffractograms were refined using the Rietveld method with the conventional reliability factors (Fullprof program package). Unit cell parameters, atomic positions, occupancies and Debye–Waller factors were refined on the basis of the $Fd\bar{3}m$ space group corresponding to the spinel structure (and for co-precipitation compounds the ZnO phase was added). Fullprof peak profile function No. 7 was used, and the crystallite size was directly obtained.

3 SEM analysis

SEM micrographs were recorded with a HITACHI 4500-I apparatus equipped with a field-emission gun (SEM-FEG) working at 3.0 kV. Such equipment allowed a high spatial resolution (approximately 5 nm) while operating at low accelerating voltages.

4 Photoluminescence analysis

Excitation spectra were recorded with the spectrofluorimeter SPEX FL212 (450 W, xenon lamp) and corrected for the variation of the incident flux. Emission spectra were corrected for the transmission of the monochromator and the response of the photomultiplier. This equipment was also used to record the diffuse reflectance spectra. A black reference (B: blacktoner) and a white reference (W: Magnesia MgO) were scanned under identical conditions and the measurement from the sample (S) was corrected with the following relation, in order to obtain the desired data (D): $D = (S - B)/(W - B)$.

Results and discussion

1 Structural characterization

The X-ray analysis of the green product (raw precipitate), obtained by co-precipitation synthesis, shows the presence of NH_4NO_3, which can be removed by washing. The amorphous behaviour of the raw precipitate is a clear indication of the homogeneity of the mixture between zinc oxide and aluminum hydroxide, which avoids separate crystallisation.

The amorphous precipitate transforms into the $ZnAl_2O_4$ spinel phase after thermal treatment under air at temperatures between 600 °C and 1200 °C. Rietveld refinements allowed the determination of numerous parameters such as the cell parameter, the inversion rate and the crystallite size, depending on the thermal treatment temperature. These results and the reliability factors of the refinement are reported in Table 1. The experimental, calculated and difference spectra are shown in Fig. 3 for the two synthesis temperatures of 600 °C and 1200 °C. It should be noted that ZnO was detected as an impurity in the X-ray diffractogram of the sample prepared at the highest synthesis temperature. These impurity peaks are evident in the inset of Fig. 3. The presence of traces of zinc oxide results from the difficulty in adjusting the Zn/Al stoichiometry inside the precipitate due to the amphoteric behaviour of the zinc oxide and the aluminum hydroxide in aqueous solution. Hence, this process unfortunately cannot guarantee a pure spinel form. Even if the ZnO impurity could be selectively dissolved by post-washing with a slightly acidic aqueous solution, the Zn : Al stoichiometry inside the spinel lattice may deviate from the target 1 : 2 ratio due to the initial excess of zinc in the starting

amorphous precipitate. However, this process offers the possibility of varying the crystallite size of the spinel compound over a very large range: from 5 nm to more than 100 nm via control of the final treatment temperature.

Table 1 Inversion model: structural parameters of $ZnAl_2O_4$ synthesized through the co-precipitation route as a function of the heat treatment temperature

				Reliability factors[b]			
Synthesis T°	Crystallite size (nm)	Cell parameter (Å)	Inversion rate[a] (%)	Phase	R_p	Chi^2	Bragg R-factor
Co-p 600 °C	4.7	8.08(3)	17.1	Spinel	6.28	6.97	4.03
Co-p 800 °C	20.3	8.08(7)	4.4	Spinel	4.38	1.78	1.48
				ZnO			0.276
Co-p 1000 °C	57.8	8.086(3)	4.3	Spinel	5.39	1.71	1.00
				ZnO			0.145
Co-p 1200 °C	119.4	8.087(3)	4.8	Spinel	7.75	1.94	1.96
				ZnO			0.191

[a] Zn in the octahedral site. [b] With all non-excluded and not corrected for background.

Using the Pechini process, a pure spinel phase can be obtained over the same range of temperatures as with co-precipitation, starting from 600 °C. The same parameters describing the structural and morphological properties were analysed by X-ray diffraction; the results are reported in Table 2. For illustration, Rietveld refinements of the 600 °C and 1200 °C samples are reported in Fig. 4.

The crystallite size determined from the peak profile refinements varies over a narrower range than from the co-precipitation process (from 20 nm to 120 nm). Crystallites smaller than 10 nm in diameter cannot be obtained by the Pechini synthesis. Nevertheless, no trace of impurity is observed in the X-ray patterns of samples obtained, regardless of the synthesis temperature.

The SEM images provided a direct illustration of the morphology of the powder samples as a function of the synthesis temperature and are shown for both processes in Fig. 5. It can be clearly seen from the SEM photographs that the crystallite size of the low synthesis temperature (600 °C) products varies between the two synthetic routes. At 1200 °C, the crystallite sizes are equal whatever the synthetic route chosen (~120 nm for both synthesis temperatures), due to the advanced degree of sintering that occurs at such high temperatures. Moreover, the presence of two phases for the 1200 °C sample obtained from the co-precipitation process is clearly observed: besides the large crystallites of the main phase of $ZnAl_2O_4$, crystallites of approximately 100 nm of diameter are observed, attributed to the zinc oxide.

Hence, the co-precipitation process has the advantage of greater control of the spinel crystallite size obtained (to our knowledge, 5 nm $ZnAl_2O_4$ crystals cannot be found in the literature), but the perfect stoichiometry of the Zn/Al ratio is not necessarily maintained, as observed with the occurrence of ZnO impurities. The Pechini route also allows control of the crystallite size, and adds the advantage of recovering pure $ZnAl_2O_4$ no matter the synthesis temperature used.

2 Cation distribution and its correlation to the synthetic procedure

At this stage, it is interesting to correlate the inversion rate and/or the morphology of the spinel to the synthesis temperature for both synthetic routes. An asymptotic decrease of the inversion rate versus the synthesis temperature is observed for both processes (Fig. 6). That means that the key parameter which governs the value of δ is not expressly the crystallite size but the synthesis temperature. In fact, equal inversion rates are obtained for a 5 nm sample and a 23 nm sample prepared by the co-precipitation and Pechini routes, respectively. In this comparison, the smallest crystallite is obtained at the lowest temperature. The asymptotic decrease of the inversion rate versus the synthesis temperature is in good agreement with previous results reported in the literature on $ZnAl_2O_4$ (ref. 40) and the analogous $CoAl_2O_4$ spinel compounds.[8,41–47]

Table 2 Inversion model: structural parameters of $ZnAl_2O_4$ synthesized through the Pechini route as a function of the heat treatment temperature

				Reliability factors[b]		
Synthesis T°	Crystallite size (nm)	Cell parameter (Å)	Inversion rate[a] (%)	R_p	Chi^2	Bragg R-factor
Pec 600 °C	32.4	8.08(9)	8.7	6.70	5.04	2.60
Pec 800 °C	41.5	8.09(5)	5.9	5.76	4.00	2.77
Pec 1000 °C	54.9	8.084(5)	4.8	6.10	3.77	2.25
Pec 1200 °C	115.6	8.089(4)	4.7	8.45	2.50	2.79
Pec 1350 °C	119.3	8.087(4)	2.6	12.1	2.18	3.90

[a] Zn in the octahedral site. [b] With all non-excluded and not corrected for background.

A final point is the observation of a second type of structural defect in the pure spinel compounds obtained from the Pechini route. Significant electron density residues are observed at the empty positions, extracted from differential Fourier cartographies between calculated and experimental signals (Fig. 7). The main electron density residues are located at the 16c Wyckoff position with (0, 0, 0) coordinates. This Wyckoff position corresponds to the empty octahedral sites of the spinel matrix. The six oxygen ligands are located at this position centre at 2.1441(8) Å. A simulated valence calculation from Brown and Altermatt[48] on this position for Zn^{2+} and Al^{3+} indicates without ambiguity that Zn^{2+} is the cation occupying this interstitial position. New refinement iterations were performed taking into account these supplementary zinc cations in the (0, 0, 0) position, with a variable occupation rate to refine occupancy. The refinement results, which are reported in Table 3, show a direct correlation between the site occupancy and the synthesis temperature. An asymptotic decrease of the occupancy can be positively correlated to the inversion rate and/or the synthesis temperature.

Table 3 Inversion with the interstitial Zn model: structural parameters of $ZnAl_2O_4$ synthesized through the Pechini route as a function of the heat treatment temperature

				Reliability factors[b]		
Synthesis T°	Crystallite size (nm)	Cell parameter (Å)	Inversion/interstitial rate[a] (%)	R_p	Chi^2	Bragg R-factor
Pec 600 °C	32.4	8.08(9)	Zn[6] 7.55/Zn_i 0.72	6.69	5.05	2.63
Pec 800 °C	41.5	8.09(5)	Zn[6] 5.01/Zn_i 1.14	5.73	4.08	2.46
Pec 1000 °C	55.0	8.084(5)	Zn[6] 3.73/Zn_i 0.79	6.06	3.77	1.97
Pec 1200 °C	115.6	8.089(4)	Zn[6] 2.93/Zn_i 0.07	8.52	2.53	2.96
Pec 1350 °C	119.3	8.087(4)	Zn[6] 1.35/Zn_i 0.07	12.1	2.18	3.90

[a] Zn in the octahedral site. [b] With all non-excluded and not corrected for background.

Thus, variation of the synthesis temperature is linked to the crystallite size of the $ZnAl_2O_4$ compounds and enables control over the inversion rate of the Zn^{2+} and Al^{3+} cations inside the spinel crystallographic network, as previously shown in the literature.[40] Furthermore, the accurate comparison of the results obtained from the two "chimie douce" processes has shown that the inversion rate is actually controlled by the synthesis temperature rather than the crystallite size. Finally, the pure spinel phase obtained via the Pechini route over a large range of synthesis temperatures leads to high quality X-ray diffraction pattern refinements and Fourier differential maps. In addition to the cationic inversion phenomenon between the 8a and 16d sites, these analyses have shown that the synthesis at low temperatures generates a significant presence of Zn^{2+} ions in interstitial positions as defects.

It is interesting to note that the last refinement series can be made without considering any inversion rate. Indeed, it can be proposed that the inversion rate is actually an artefact resulting from the lack of consideration of vacancies that are mainly located at the tetrahedral sites of the structure. This is an extreme point of view, but the vacancies should at least have some effect on the inversion rate. The formula $Zn_{1-3x}[Zn_{2x}Al_{2-2x}]O_{4-4x}$ was envisaged on the basis of the chemical composition, complete filling of the octahedral sites and the oxide electroneutrality. A partial occupation of the octahedral sites by Zn^{2+} must be considered. There is the same number of adjustment parameters in the latter case as for the inversion rate model: the x variable directly replaces the inversion rate. The refinement results performed considering a tetrahedral vacancy rate of 3x are reported in Table 4. The correlation factors are on the same order as in previous models. Hence, the consideration of vacancies segregated inside the tetrahedral positions leads to the same results as those obtained with the partial inversion rate of Zn^{2+} ions. The occurrence of both cationic and anionic vacancies cannot be rejected and should also be considered.

Table 4 Vacancy model: structural parameters of $ZnAl_2O_4$ synthesized through the Pechini route as a function of the heat treatment temperature

				Reliability factors[b]		
Synthesis T°	Crystallite size (nm)	Cell parameter (Å)	Td vacancy rate[a] (%)	R_p	Chi^2	Bragg R-factor
Pec 600 °C	32.4	8.08(9)	6.48	6.71	5.07	2.61
Pec 800 °C	41.5	8.09(5)	4.13	5.74	4.11	2.45
Pec 1000 °C	55	8.084(5)	3.05	6.09	3.79	2.23
Pec 1200 °C	115.6	8.089(4)	3.25	8.36	2.49	2.47
Pec 1350 °C	119.3	8.087(4)	1.28	12.1	2.18	3.92

[a] Vacancy at the tetrahedral site. [b] With all non-excluded and not corrected for background.

3 Luminescence characterisation and thermal probe behavior

The optical properties of the spinel matrix obtained through the Pechini synthetic route were studied as a function of the heat treatment of the materials. As the results obtained from both synthetic routes are equivalent, we limit the discussion of the optical properties to the Pechini prepared samples. The diffuse reflectance spectra are shown in Fig. 8. The increase of the heat treatment temperature from 600 °C to 1200 °C leads to a strong reduction of the absorption band between 300 nm and 360 nm. This band in the 1350 °C heat treated sample is very weak, which indicates that this absorption is related to the existence of Zn_{Al} or Al_{Zn} antisite defects (six-fold coordinated Zn^{2+} and four-fold coordinated Al^{3+}) in the indirect spinel lattice.

The spectral distributions of the excitation and emission bands were examined at high (254–270 K) and low temperatures (10 K). Fig. 9a–d show the results obtained for two specific samples. The spectral distribution of the 1200 °C heat treated material corresponds to the indirect spinel structure. The 1350 °C heat treatment stabilised the nearly direct spinel, as demonstrated previously. The strongest variation of the optical properties is obtained for these two thermal treatment temperatures.

For the 1200 °C heat treated sample, there is a strong emission band at 610 nm (Fig. 9a) upon excitation at 370 nm. This emission is partially quenched at room temperature and shifted to higher energy at higher temperatures (580 nm for T > 250 K). Groups of lines can also be distinguished at approximately 688 nm. This red photoluminescence is due to the E_g-$^4A_{2g}$ R-, N-zero phonon lines of trivalent chromium at the octahedral site of the aluminium ions[49] (Fig. 10). The emission spectra also contain satellite lines distributed around the main peak, which can be identified as vibronic (phonon assisted transitions) sideband transitions of Cr^{3+} ions. The presence of chromium impurities in aluminium compounds is often observed due to trace impurities in the precursor materials. For excitation at higher energy (λ_{ex} = 235 nm), an additional band is detected at approximately 460 nm (Fig. 9c and d). This band is also affected by the temperature. Two thin lines can be distinguished at 368 nm and 372 nm. The first one can be attributed to a direct electron–hole pair recombination, or excitonic emission. The corresponding energy (3.3 eV) is slightly lower than that of the band gap value of $ZnAl_2O_4$ (3.8 eV).[50] This indicates the existence of an intermediary energy level (level 1) below the conduction band in which the electron is trapped before radiative recombination with a hole in the valence band or in a shallow level above the valence band (level 2) (see Fig. 11). As the energy difference between the two lines is weak (0.03 eV or 492 cm^{-1}), the second line may be due to another self-trapped exciton recombination or may be a phonon replica emission of the first self-trapped excitonic line. This electron–phonon coupling is commonly observed at low temperatures in ZnO wurtzite type structures.[51,52]

The intensities of the 460 nm and 610 nm bands collapse after the 1350 °C heat treatment. Indeed, the second one cannot be detected anymore upon excitation at 235 nm. As discussed previously, one of the interesting properties of the spinel compound is the possibility to obtain and to control a high degree of disorder in the cation sub-lattice (the inversion rate). The reciprocal exchange of Zn^{2+} ions and Al^{3+} ions between octahedral and tetrahedral positions creates the existence of Zn_{Al} or Al_{Zn} antisite defects. This leads to the stabilisation within the lattice of local defects which are responsible for the spectroscopic features of this material. Many studies have reported on the intrinsic emission of spinel (natural mineral gahnite or a synthetic single crystal, ceramics) under ionising radiation and X-ray excitation.[53–56] In the indirect spinel, Zn^{2+} ions are located at the octahedral lattice sites and form centres with excess negative charge. During high irradiation, the capture of a free hole by this site neutralises the defect. A complementary process is observed by the capture of a free electron by the excess positive charge of an Al^{3+} ion. A neutral centre can be obtained as given by the following equation:

$$[Zn_{Al}^{2+}]^{-} + h^{+} \rightarrow [Zn_{Al}^{2+}]^{0}$$

$$[Al_{Zn}^{3+}]^{+} + e^{-} \rightarrow [Al_{Zn}^{3+}]^{0}$$

Because of the low electron affinity of Al^{3+} ions, the captured electron may leave its trap and finally recombine with a nearby trapped hole.[55] These processes result in a radiative emission at approximately 255 nm. F-centres can also be responsible for emission bands at approximately 360 nm.[55,56] In the present study, the excitation energy is not sufficient to observe such emissions, which correspond to energy larger than the bandgap. Moreover, the two visible bands are strongly dependent on the inversion rate of the spinel lattice. Their origin is then related to the existence of antisite defects and all the processes that occur under irradiation to stabilise the system. Other defects may also cause radiative emission in the visible range. On the one hand, an oxygen vacancy $V_O^{\cdot\cdot}$ in the vicinity of the octahedral antisite of Zn^{2+} ions might favor a hole trapping process, contributing to the neutralisation of the negatively charged site. This could generate the existence of a shallow level located below the conduction band (level 1'). On the other hand, a hole centre may be created by capturing another hole at the oxygen vacancy site according to the following equation:

$$V_O^{2-} + h^+ \rightarrow V_O^-$$

This will constitute a deep hole trapped level within the gap of the material (level 2'). One can imagine that a photogenerated electron in the conduction band or level 1' can recombine with the deep hole trapped level 2', giving rise to the 585 nm emission. We propose here a parallel between the reported visible emission of the as-synthesised spinel material and that of ZnO. Visible emission has been intensively studied in ZnO wurtzite type structures prepared by sol gel techniques, organometallic methods or other soft chemistry synthetic routes.[57–59] In this compound, Zn^{2+} ions are located in a tetrahedral environment. ZnO is a direct semiconductor whose gap is comparable to that of spinel (3.37 eV and 3.8 eV, respectively). A yellow-green emission ranging from 500 nm to 600 nm has been reported by D. Hahn et al.[60] An explanation of this process was given by A. Van Dijken et al.,[61] as being due to the recombination of a shallowly trapped electron with a deeply trapped hole. In this process, surface defects such as non-bridging O^{2-}/O^- trapped the photogenerated hole, which then migrated to a vacancy positioned deeper in the particle. The resulting deep hole trapped level is then located in the band gap of the semiconductor, above the valence band. The photogenerated hole trapped in the deep oxygen vacancy level recombines with the photogenerated electron trapped in the shallow level located below the conduction band, giving rise to the yellow-green luminescence. We propose the assignation of the 610 nm band to a radiative process involving an oxygen vacancy (1'–2' radiative recombination route) (Fig. 11). This radiative process is complex and probably linked to the existence of two energy levels 1'a and 1'b below the conduction band. At low temperatures, the 1'a–2' electronic transition occurs, but an increase in the temperature results in a thermal equilibrium between 1'a and 1'b. The emission is then due to the 1'b–2' electron transition, leading to a blueshift of the band. Because similar emission is seen with ZnO,[62] the origin of the blue emission (460 nm) may be related to the interstitial zinc ions in the spinel lattice. Blue luminescent centres have also been reported in ZnO,[63] and investigated by full-potential linear Muffin-tin orbital calculation published by P.S. Xu et al.[64] The authors positioned the interstitial zinc defect energy level 2.9 eV above the valence band, making it a shallow level below the conduction band. The corresponding energy is of the same order of magnitude as the radiative de-excitation observed in Fig. 9. Considering the structural refinement described previously and the high probability of interstitial zinc ions in the spinel lattice, the blue luminescence may reflect the contribution of these defects to the radiative processes (1''–2'' radiative recombination route). Radiative recombination pathways are depicted in Fig. 11. Note the existence of the N-line of trivalent chromium that seems to confirm (according to W. Zang et al.) the contribution of Cr^{3+} ions to nearby interstitial zinc ions (results observed for $ZnGa_2O_4$ spinel nano-sized phosphors[65]).

Conclusion

We have demonstrated that the main factor governing the inversion rate of $ZnAl_2O_4$ is not the crystallite size but the thermal history of the sample. The co-precipitation synthesis led to a larger crystallite size distribution, but with heat treatments above 800 °C, equivalent inversion rates are obtained for both the Pechini and co-precipitation syntheses.

For samples treated at low synthesis temperatures, the optical properties point to three types of defects responsible for the radiative emission bands: Zn_{Al} antisites (linked to the partial inversion rate), oxygen vacancies and Zn^{2+} ions in interstitial positions. Drastic decreases of the associated emission intensities between the 1200 °C and the 1350 °C heat-treated samples confirm that these emissions are caused by various defects. From the X-ray diffraction results and from previous studies on the ZnO wurtzite phase, the two groups of emission bands located at 460 nm and 610 nm were attributed to Zn^{2+} ions in interstitial positions and oxygen vacancies resulting from the existence of Zn_{Al} antisites, respectively.

Finally, we successfully correlated the optical properties and the structural evolution (disappearance of antisites and non-stoichiometric defects) to the synthesis temperature of the as-prepared $ZnAl_2O_4$ spinels, making $ZnAl_2O_4$ a good candidate for an optical thermal history sensor.

Acknowledgements

Lucile Cornu is the holder of the doctoral fellowship supported by the Bordeaux 1 University. The authors thank CNRS, the Aquitaine région and the ANR (ANR-2010-BLANC-0820) for financial support.

References

1. C. A. Leech and L. E. Campbell, Adv. Chem. Ser., 1975, 77, 143–161.
2. J. Wrzyszcz, M. Zawadzki, J. Trawczynski, H. Grabowska and W. Mista, Appl. Catal., A, 2001, 269, 210–263.
3. P. Mierczyński, W. Maniukiewicz, D. Gebauer, W. K. Jozwiak and T. P. Maniecki, Kinet. Catal., 2009, 50(2), 228–234.
4. B. B. Dantas, N. A. S. Nogueira, J. M. Sasaki, N. L. Freitas, R. H. G. A. Kiminami, A. C. F. M. Cost and K. M. S. Viana, Mater. Sci. Forum, 2010, 660–661, 52–57.
5. S. K. Sampath and J. F. Cordaro, J. Am. Ceram. Soc., 1998, 81, 649–654.
6. T. K. Parya, R. K. Bhattacharyya, S. Banerjee and U. B. Adhikari, Ceram. Int., 2010, 36(4), 1211–1215.
7. J.-M. Wu, W.-Z. Lu, W. Lei and X.-C. Wang, Mater. Res. Bull., 2011, 46(9), 1485–1489.
8. C. Angeletti, F. Pepe and P. Porta, J. Chem. Soc., 1977, 73, 1972–1977.
9. X. Li, Z. Zhu, Q. Zhao and L. Wang, J. Hazard. Mater., 2011, 186(2–3), 2089–2096.
10. Z. Zhu, Q. Zhao, X. Li, H. Li, M. Tade and S. Liu, Catal. Sci. Technol., 2013, 3, 788–796.
11. A. C. F. M. Costa, R. H. G. A. Kiminami, P. T. A. Santos and J. F. Silva, J. Mater. Sci., 2013, 48(1), 172–177.
12. I. Alekseeva, O. Dymshits, V. Ermakov, V. Golubkov, A. Malyarevich, M. Tsenter, A. Zhilin and K. Yumashev, Phys. Chem. Glasses: Eur. J. Glass Sci. Technol., Part B, 2012, 53(4), 167–180.
13. S. Yoo, U.-C. Paek and W.-T. Han, J. Non-Cryst. Solids, 2002, 303(2), 291–295.
14. X. Duan, D. Yuan, X. Cheng, Z. Sun, H. Sun, D. Xu and M. Lv, J. Phys. Chem. Solids, 2003, 64(6), 1021–1025.
15. A. Fernández-Osorio, D. Hernández-Mendoza and E. Pineda-Villanueva, in 2010 Nanotechnology 2010: Advanced Materials, CNTs, Particles, Films and Composites – Technical Proceedings of the 2010 NSTI Nanotechnology Conference and Expo, NSTI-Nanotech, 2010.
16. G. Lorenzi, G. Baldi, F. Di Benedetto, V. Faso, P. Lattanzi and M. Romanelli, J. Eur. Ceram. Soc., 2006, 26(3), 317–321.
17. L. Gama, M. A. Ribeiro, B. S. Barros, R. H. A. Kiminami, I. T. Weber and A. C. F. M. Costa, J. Alloys Compd., 2009, 483(1–2), 453–455.
18. V. Singh, R. P. S. Chakradhar, J. L. Rao and H.-Y. Kwak, J. Mater. Sci., 2011, 46(7), 2331–2337.
19. H. H. Luc, T. K. Nguyen, V. M. Nguyen, A. Suchocki, A. Kamińska, V. K. Le, V. H. Nguyen and T. Luong, Acta Phys. Pol., A, 2003, 104(6), 581–587.
20. J. Derkosch and W. Mikenda, J. Lumin., 1983, 28(4), 431–441.
21. M.-T. Tsai, Y.-S. Chang, I.-B. Huang and B.-Y. Pan, Ceram. Int., 2013, 39, 3691–3697.
22. P. T. A. Santos, C. M. Furtado, M. O. Rodrigues and A. C. F. M. Costa, Mater. Sci. Forum, 2012, 727–728, 1119–1124.
23. C. M. Furtado, P. M. A. G. De Araújo, P. T. A. Dos Santos and A. C. F. M. Costa, Mater. Sci. Forum, 2012, 727–728, 263–268.
24. I. Miron, C. Enache, A. Dabici and I. Grozescu, J. Optoelectron. Adv. Mater., 2012, 14(9–10), 820–825.
25. I. Miron, C. Enache, M. Vasile and I. Grozescu, Phys. Scr., T, 2012, 149, 014064/1–014064/3.
26. G. D. Price, S. L. Price and J. K. Burdett, Phys. Chem. Miner., 1982, 8, 69–76.
27. J. Popovic, B. Grzeta, B. Rakvin, E. Tkalcec, M. Vrankic and S. Kurajica, J. Alloys Compd., 2011, 509, 8487–8492.
28. R. F. Cooley and J. S. Reed, J. Am. Ceram. Soc., 1972, 55, 395–398.
29. J. Popovic, E. Tkalcec, B. Grzeta, S. Kurajica and B. Rakvin, Am. Mineral., 2009, 94, 771–776.
30. J. C. Waerenborgh, M. O. Figueiredo, J. M. P. Cabral and L. C. J. Pereira, J. Solid State Chem., 1994, 111, 300–309.
31. S. Mathur, M. Veith, M. Haas, H. Shen, N. Lecerf, V. Huch, S. Hufner, R. Haberkorn, H. P. Beck and M. Jilavi, J. Am. Ceram. Soc., 2001, 84, 1921–1928.
32. A. Le Nestour, Ph.D. Thesis, Université Bordeaux 1, 2006 .
33. H. Matsui, C.-N. Xu, Y. Liu and H. Tateyama, Phys. Rev. B: Condens. Matter Mater. Phys., 2004, 69, 235109/1–235109/7.
34. N. J. van der Laag, M. D. Snel, P. C. M. M. Magusin and G. de With, J. Eur. Ceram. Soc., 2004, 24, 2417–2424.
35. M. Vasile, P. Vlazan and N. M. Avram, J. Alloys Compd., 2010, 500, 185–189.
36. L. Torkian, M. M. Amini and Z. Bahrami, Wuji Cailiao Xuebao, 2011, 26, 550–554.
37. V. Singh, R. P. S. Chakradhar, J. L. Rao and D.-K. Kim, J. Lumin., 2008, 128, 394–402.
38. B. S. Barros, P. S. Melo, R. H. G. A. Kiminami, A. C. F. M. Costa, G. F. Sa and S. Alves Jr, J. Mater. Sci., 2006, 41, 4744–4748.
39. M. P. Pechini, Ceramic Dielectric Materials, 1967.
40. M. Gaudon, A. Apheceixborde, M. Menetrier, A. Le Nestour and A. Demourgues, Inorg. Chem., 2009, 48, 9085–9091.
41. M. Zayat and D. Levy, Chem. Mater., 2000, 12, 2763–2769.
42. P. Garcia Casado and I. Rasines, J. Solid State Chem., 1984, 52, 187.
43. G. Monari and T. Mandefrini, Ceram. Eng. Sci. Proc., 1996, 17(1), 102–110.
44. M. Llusar, A. Forès, J. A. Badenes, J. Calbo, M. A. Tna and G. Monros, J. Eur. Ceram. Soc., 2001, 21, 1121–1130.
45. K. Hanashima, Y. Kodama, D. Akahoshi, C. Kanadani and T. Saito, J. Phys. Soc. Jpn., 2013, 82, 024702.
46. W. Li, J. Li and J. Guo, J. Eur. Ceram. Soc., 2003, 23, 2289–2295.
47. D. M. A. Melo, J. D. Cunha, J. D. G. Fernandes, M. I. Bernardi, M. A. F. Melo and A. E. Martinelli, Mater. Res. Bull., 2003, 38, 1559–1564.
48. I. D. Brown and D. Altermatt, Acta Crystallogr., Sect. B: Struct. Sci., 1985, 41, 244–247.
49. W. Mikenda and A. Preisinger, J. Lumin., 1981, 26, 53–83.
50. G. Lakshminarayana and L. Wondraczek, J. Solid State Chem., 2011, 184, 1931–1938.
51. B. K. Meyer, H. Alves, D. M. Hofmann, W. Kriegseis, D. Forster, F. Betram, J. Christen, A. Hoffmann, M. Strabβurg, M. Dworzak, U. Haboeck and A. V. Rodina, Phys. Status Solidi B, 2004, 241(2), 231–260.

52. A. Teke, Ü. Özgür, S. Dogan, X. Gu, H. Morkoç, B. Nemeth, J. Nause and H. O. Everitt, Phys. Rev. B: Condens. Matter Mater. Phys., 2004, 70, 195207/1–195207/10.
53. A. Lorincz, M. Puma, F. J. James and J. H. Crawford, J. Appl. Phys., 1982, 53, 927–932.
54. V. T. Gritsyna, Y. G. Kazarinov, V. A. Kobyakov and K. E. Sickafus, J. Appl. Spectrosc., 2004, 71(3), 395–399.
55. T. A. Bazilevskaya, V. T. Gritsyna, D. V. Orlinski, L. V. Udalova and A. V. Voitsenya, J. Nucl. Mater., 1998, 253, 133–140.
56. V. T. Gritsyna, Y. G. Kazarinov, V. A. Kobyakov and I. E. Reimanis, Nucl. Instrum. Methods Phys. Res., Sect. B, 2006, 250, 342–348.
57. V. Munoz-Sanjose, R. Tena-Zaera, C. Martınez-Tomas, J. Zuniga-Perez, S. Hassani and R. Triboulet, Phys. Status Solidi C, 2005, 2, 1106.
58. M. L. Kahn, T. Cardinal, B. Bousquet, M. Monge, V. Jubera and B. Chaudret, ChemPhysChem, 2006, 7, 2392–2397.
59. M. Singhal, V. Chhabra, P. Kang and D. O. Shah, Mater. Res. Bull., 1997, 32, 239–247.
60. D. Hahn, R. Nink and K. Tobish, Phys. Kondens. Mater., 1967, 6, 229.
61. A. van Dijken, E. A. Meulenkamp, D. Vanmaekelbergh and A. Meijerink, J. Phys. Chem. B, 2000, 104, 1715–1723.
62. C. Zhang and J. Lin, Chem. Soc. Rev., 2012, 41, 7938–7961.
63. Z. Fang, Y. Wang, D. Xu, Y. Tan and X. Liu, Opt. Mater., 2004, 26, 239–242.
64. P. S. Xu, Y. M. Sun, C. S. Shi, F. Q. Xu and H. B. Pan, Nucl. Instrum. Methods Phys. Res., Sect. B, 2003, 199, 286–290.
65. W. Zhang, J. Zhang, Z. Chen, T. Wang and S. Zheng, J. Lumin., 2010, 130, 1738–1743.

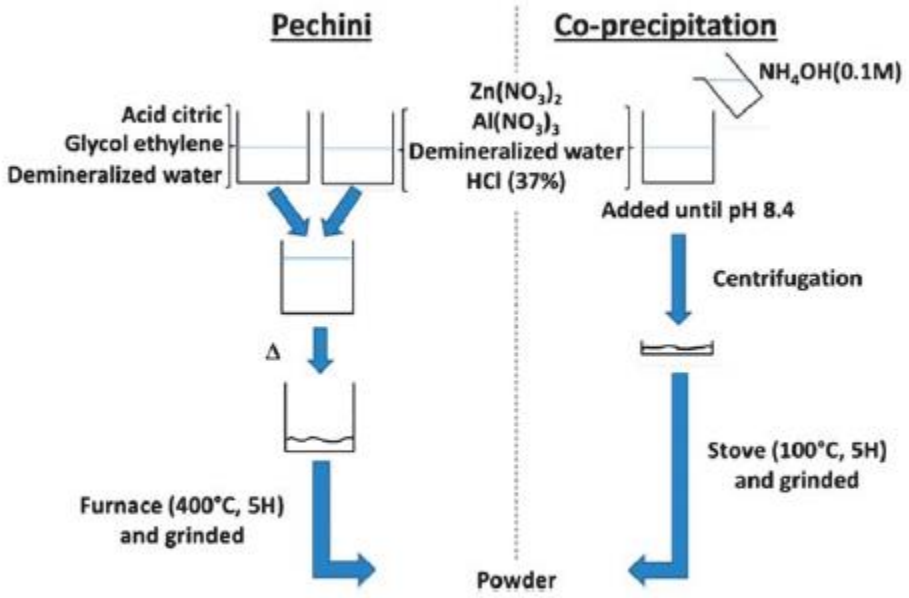

Fig. 1 Pechini and co-precipitation synthesis protocols.

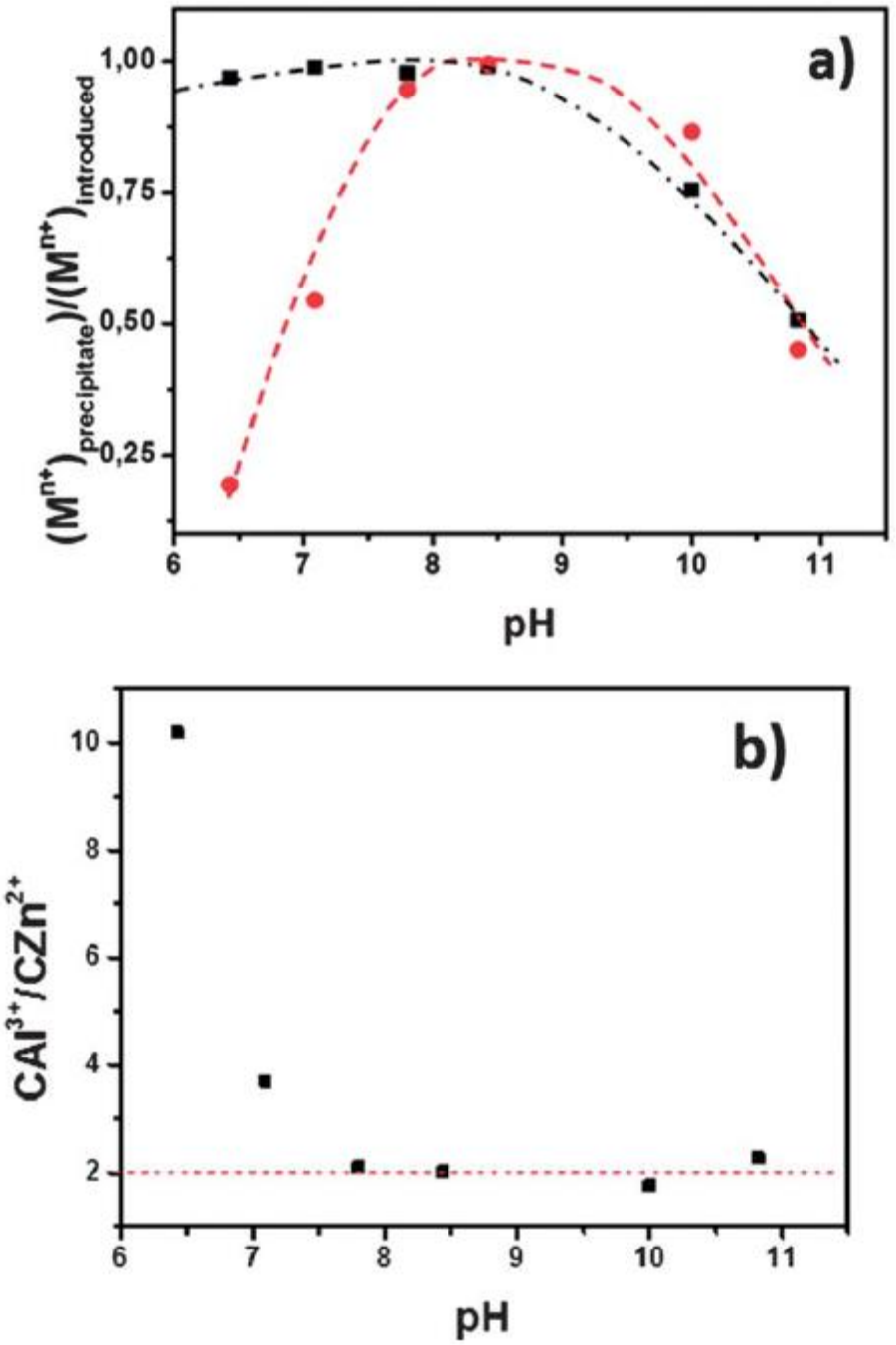

Fig. 2 (a) Ratio $[M^{n+}]_{precipitate}/[M^{n+}]_{introduced}$ *vs.* pH, Al^{3+} (black square), Zn^{2+} (red circle). (b) Ratio $[Al^{3+}]/[Zn^{2+}]$ for co-precipitation materials synthesised at various pH. The dashed red line represents the theoretical ratio.

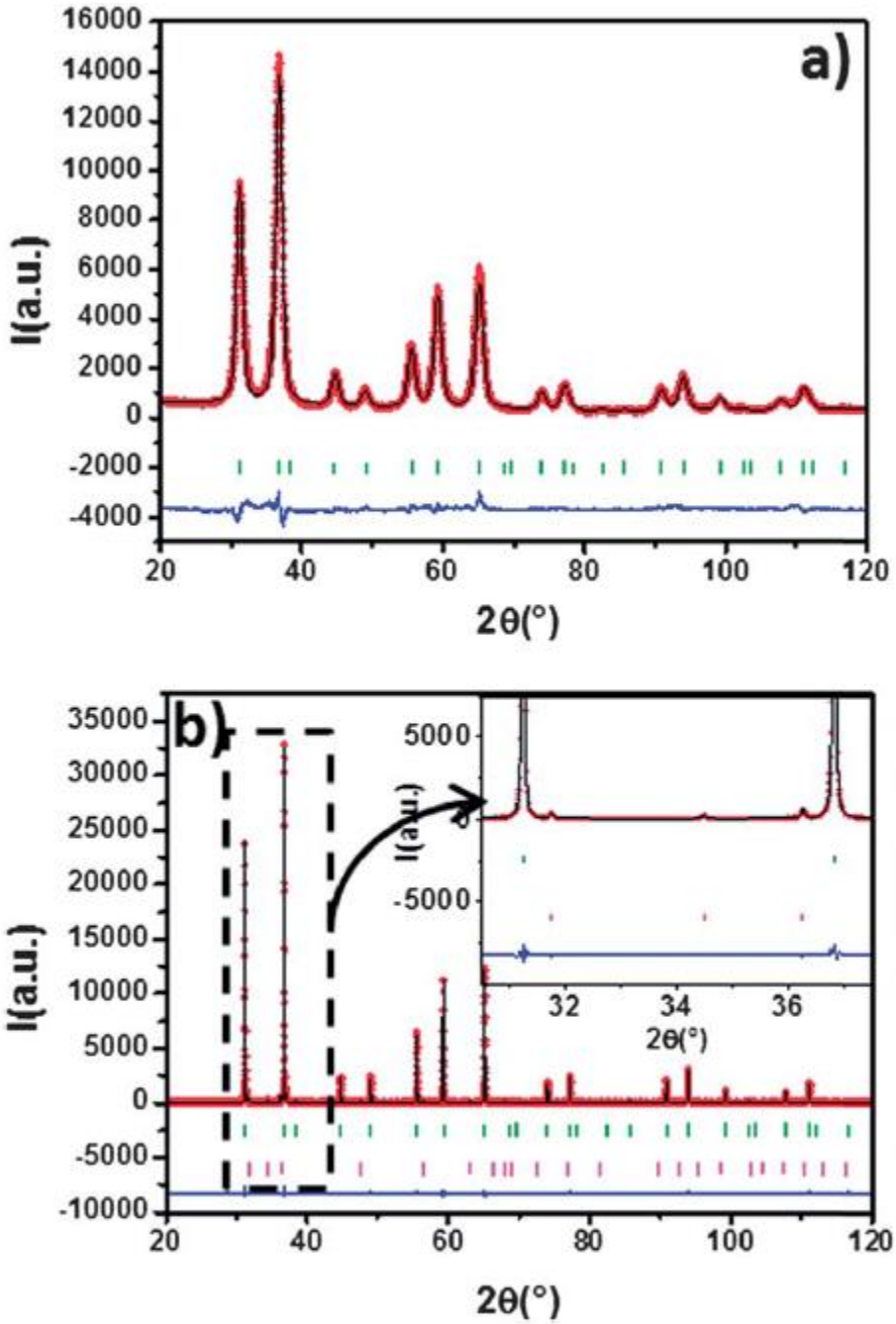

Fig. 3 Refined diffractograms for (a) co-precipitation 600 °C, (b) co-precipitation 1200 °C (green tick: theoretical diffraction peak of $ZnAl_2O_4$, pink tick: theoretical diffraction peak of ZnO).

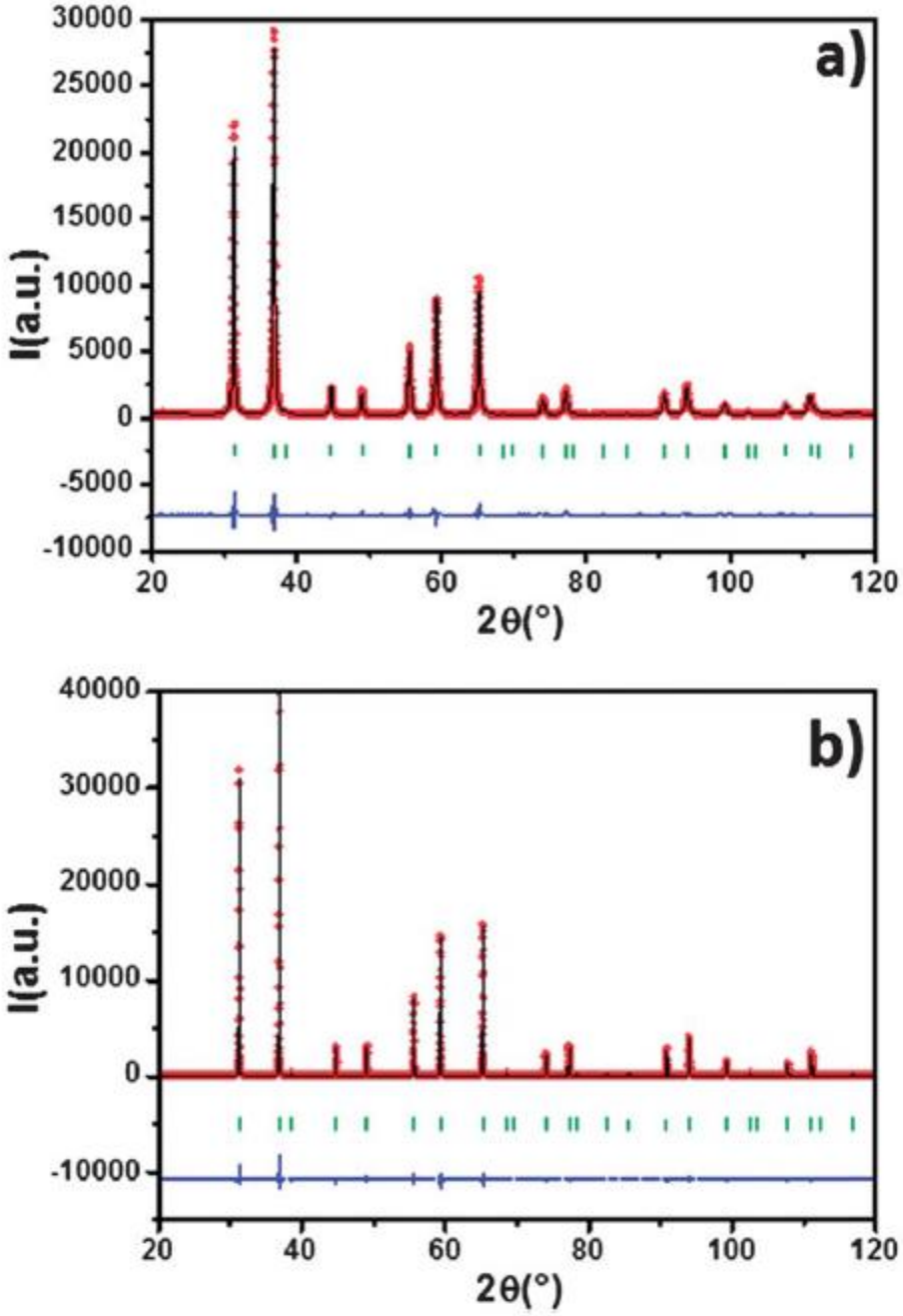

Fig. 4 Refined diffractograms for (a) Pechini 600 °C, (b) Pechini 1200 °C (green tick: theoretical diffraction peak of $ZnAl_2O_4$).

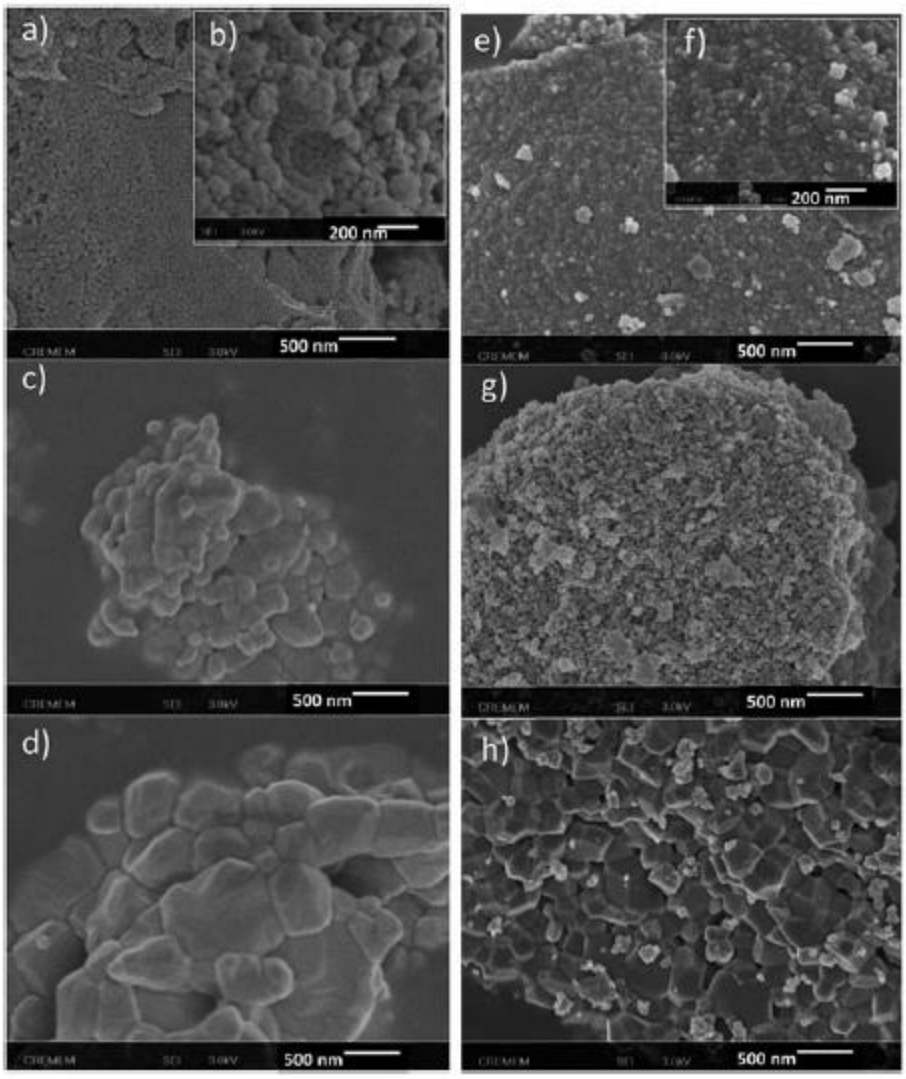

Fig. 5 SEM images for Pechini synthesis of $ZnAl_2O_4$. (a) 800 °C, (b) zoom 800 °C, (c) 1200 °C, (d) 1350 °C, and co-precipitation synthesis (e) 600 °C, (f) zoom 600 °C, (g) 800 °C, (h) 1200 °C.

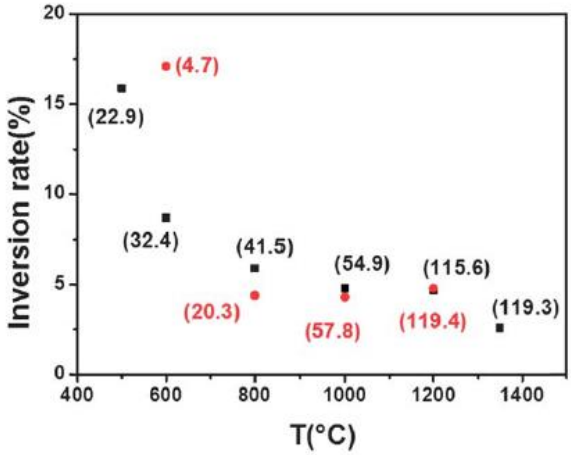

Fig. 6 Inversion rate *vs.* temperature, for co-precipitation synthesis (red circle) and Pechini synthesis (black square). Crystallite sizes of $ZnAl_2O_4$ in nm are given in parentheses.

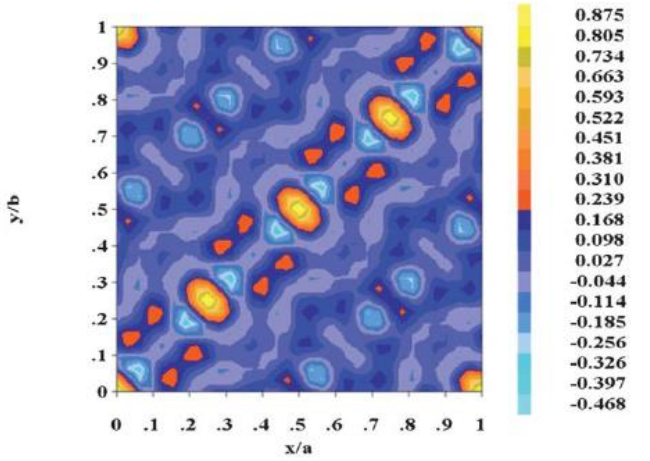

Fig. 7 Fourier map of the ($F_o - F_c$ difference) in the xy_0 plane, for the 1200 °C Pechini synthesis sample.

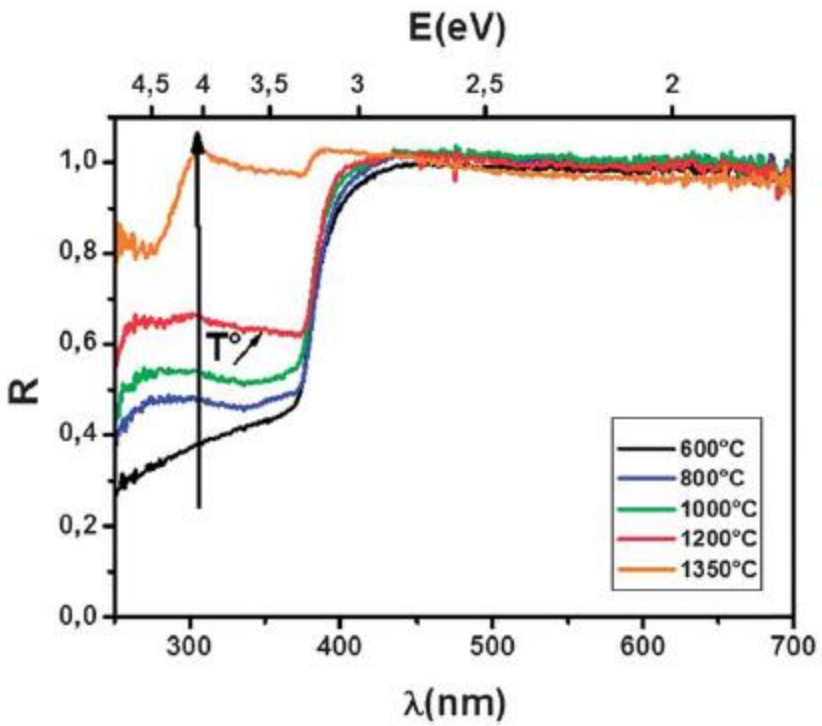

Fig. 8 Diffuse reflectance spectra of $ZnAl_2O_4$ obtained by applying several heat treatments.

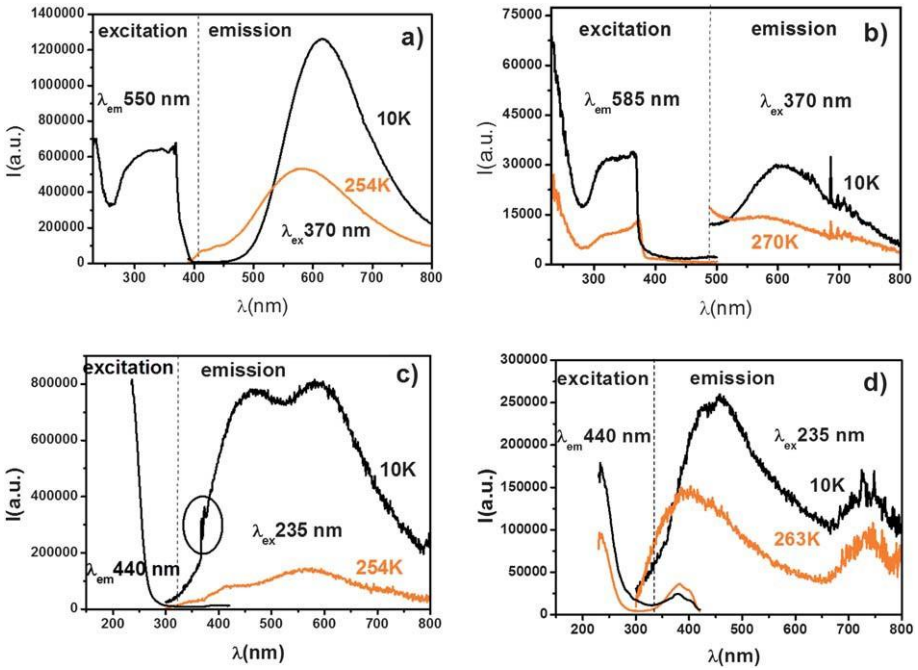

Fig. 9 Luminescence spectra of $ZnAl_2O_4$ prepared by the Pechini synthetic route: (a and c) 1200 °C heat treated sample; (b and d) 1350 °C heat treated sample.

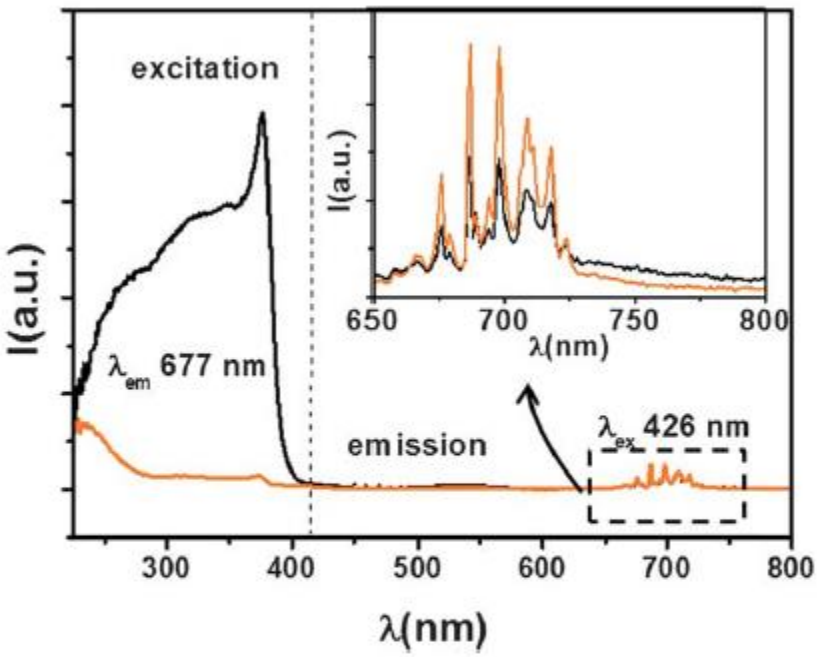

Fig. 10 Pechini 0% luminescence spectra: (a) 1200 °C heat treated sample: room temperature (black curve); (b) 1350 °C heat treated sample: room temperature (orange curve).

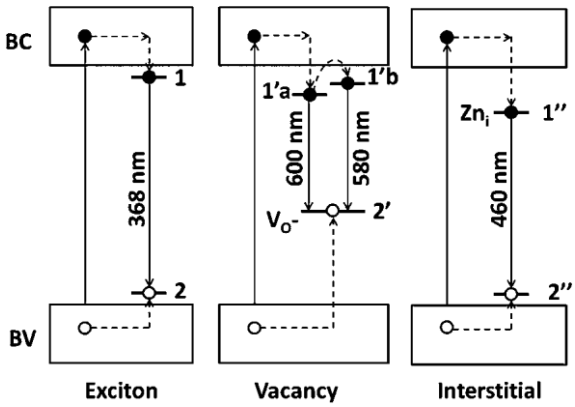

Fig. 11 Energy levels in the band gap.